Local control of cellular proliferation underlies neuromast regeneration in zebrafish

Natalia G. Lavalle[1], Jerónimo Miranda-Rodríguez[2], Emanuel Cura Costa[1], Augusto Borges[3], Oriol Viader-Llargués[3], Hernán López-Schier[3,6] & Osvaldo Chara[7,8]*

[1] *Institute of Physics of Liquids and Biological Systems (IFLySIB), National Scientific and Technical Research Council (CONICET), University of La Plata, La Plata, Argentina*

[2] *Instituto de Neurobiología, Universidad Nacional Autónoma de México (UNAM),*

[3] *Graduate School of Quantitative and Molecular Biosciences Munich (QMB), Ludwig Maximilian University, Munich, Germany*

[6] *Division of Science, New York University Abu Dhabi, Saadiyat Island, United Arab Emirates*

[7] *School of Biosciences, University of Nottingham, Nottingham, UK*

[8] *Instituto de Tecnología, Universidad Argentina de la Empresa (UADE), Ciudad Autónoma de Buenos Aires, Argentina.*

* Corresponding author

E-mail: osvaldo.chara@nottingham.ac.uk (OC)

Abstract

Biological systems are never at equilibrium but maintain stability despite perennial external disturbance. A prime example is organ regeneration, whereby despite intrinsically stochastic damage, organs are rebuilt via controlled cellular proliferation. Here, we use a mathematical approach to understand how a cell decides to re-enter and exit mitosis during organ repair. Using empirical data from regenerating neuromasts in larval zebrafish, we identify a minimal model based on ordinary differential equations (ODEs). Remarkably, the ODEs model reproduces the regeneration kinetics by assuming a cell-proliferation switch that depends on the type and the number of the neuromast cells. Additionally, a two-dimensional Cellular Potts Model (CPM) predicts that cell proliferation is a delayed response to injury. The CPM recapitulates the experimental results qualitatively and quantitatively, showing that cell proliferation is locally controlled by a switch, where each cell division stops when the type-dependent number of neighbouring cells exceeds a deterministic critical value. An intriguing corollary of our results is that a local negative feedback loop among identical cells may be a general property of organ-level proportional homeostasis.

1. Introduction

In regenerating organisms, including hydra (1–3), planaria (4,5), axolotl (6,7) and zebrafish (8), injuries that severely disrupt tissue integrity are followed by reactive cellular proliferation and tissue re-patterning. A remarkable example of this multifactorial response is found in the neuromasts of the zebrafish lateral line. These discoidal organs are composed of central mechanosensory hair cells surrounded by two types of non-sensory supporting cells, an inner population of the sustentacular cells, and an outer group of mantle cells (Fig. 1A, A'). Even after severe injuries that remove up to 95% of the constituent cells, neuromasts regenerate within one week (9). How different neuromast cells initiate and cease their mitotic activity remains unclear.

Regenerative cellular proliferation may be controlled systemically at the organismal level, globally at the tissue level, or locally within the immediacy of each cell. Here we address this question using an *in silico* morphodynamic approach (10). Specifically, we employ cell-based modelling integrating *in vivo* cellular and supracellular behaviour in regenerating neuromasts of larval zebrafish.

By developing a cell-based mathematical model, we tested the hypothesis that the neuromast-wide regenerative response is an emergent property of local cell-cell interactions. Comparing theoretical simulations with experimental data reveals that inner sustentacular cells, the main drivers of organ regeneration, cease to proliferate when they become surrounded by three or more cells of the same type, whereas mantle cells arrest divisions when confronted by between zero and two neighbouring mantle cells, indicating cooperative control of cell proliferation.

2. Results

2.1 Controlled proliferative response during neuromast regeneration in the zebrafish is consistent with a cooperative model of cell proliferation

Severe injury of zebrafish neuromasts that removes up to 95% of their cellular content is followed by an impressive regenerative response driven by the proliferation of the remaining mantle and sustentacular cells (9). To quantitatively investigate the mechanisms responsible for this regenerative response, we conceived a minimal mathematical model describing the time course of cells for each of the three cell types composing the neuromast.

Experimental observations shown that, after injury, surviving mantle cells divide to produce more mantle cells. By contrast, sustentacular-cell proliferation produces offspring of all three identities. With biased probabilities, sustentacular cells divide symmetrically to produce two sustentacular, two hair cells, two mantles, or asymmetrically to give rise to one sustentacular and one mantel cell (9). Therefore, the outcome of a sustentacular-cell division can be expressed as (Fig. 1B):

$$p_{SS} + p_{HH} + p_{MM} + p_{SM} = 1 \qquad \text{(Eq. 1)}$$

Where p_{SS}, p_{HH}, p_{MM} and p_{SM} are the probabilities that after a division, a sustentacular cell gives rise to two sustentacular cells, two hair cells, two mantle cells, or one sustentacular and one mantle cell, respectively.

We encoded the processes of cell proliferation and differentiation in a system of ordinary differential equations describing the time course of the number of cells for each cell type (see details of the model in the Computational Methods section 4.1). To prevent the number of cells from increasing indefinitely, we also assumed that the proliferation rate of sustentacular and mantle cells is controlled by the total number of sustentacular and mantle cells, respectively. In particular, we assumed that the proliferation rate of both cells decreases with a Hill-like expression, whose relevant parameters are: 1) the Hill coefficient h (considered identical for both cell types), 2) the maximal proliferation rates v (for sustentacular cells) and fv (for mantle cells), and 3) S_{50} as well as M_{50}, the number of sustentacular and mantle cells, respectively, to render 50% of the maximal proliferation rate. While the above-mentioned probabilities and the ratio between the maximal proliferation rates of sustentacular and mantle cells f were fixed from previous empirical data (Table S1, (9)), v, h, S_{50} and M_{50} are unknown parameters.

To evaluate the plausibility of this model and obtain an estimate of the unknown parameters, we fitted the model to previous measures of the time evolution of the number of hair, sustentacular and mantle cells after injury (9) (Supp. Fig. S1). Our model was able to predict the organ recovery curves, suggesting a possible mechanism for the proliferative response subjected to a control mediated by the number of cells (Fig. 1C). We estimated the unknown parameters from their best-fitting values (see Table S2): the Hill coefficient, h, *is approximately* 30, indicating a strong sigmoidal character of the proliferation rate of both cell types. This suggests a cooperative control of cell proliferation might be at play (Fig. 1D). Moreover, M_{50} and S_{50} parameters were approximately 10 and 20 respectively, reflecting the bigger number of sustentacular cells.

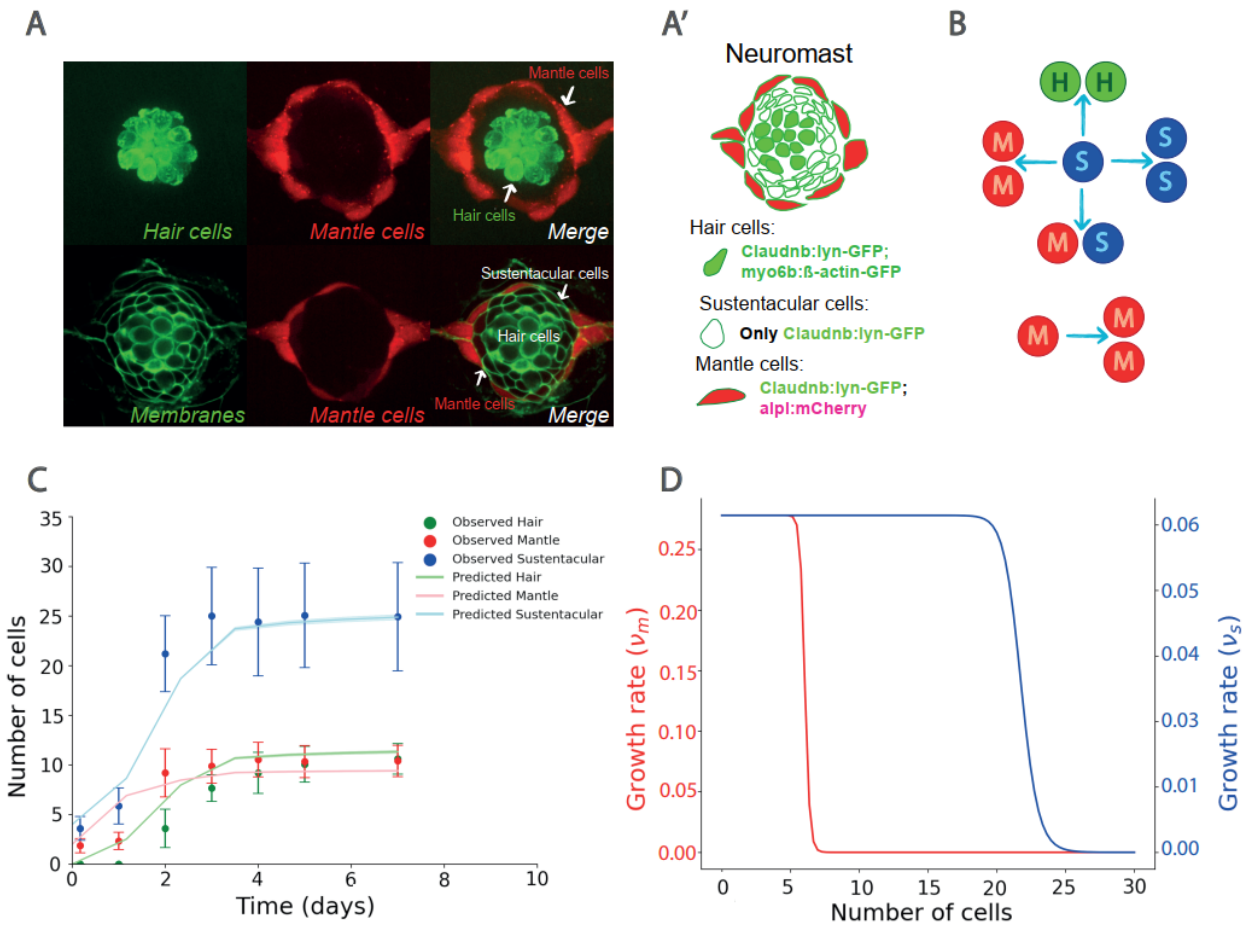

Figure 1. A) The three main cell type classification in the neuromast organ are organized radially: hair cells are located centermost; mantle cells delimit the organ peripherally while support cells fill the space between the previous two. The cells can be distinguished in vivo by looking at fluorescent transgenic markers. **A')** Hair cells are uniquely marked by a β-actin-GFP fusion under transcriptional control of the myo6b promoter. Mantle cells are specifically marked by the red fluorescent protein mCherry in the alpl:mCherry transgenic. Last, the transgenic Cldb:lyn-EGFP marks the membranes of all three cell types in the organ. A triple transgenic allows to segment the membranes of all cells and to unequivocally determine the cell type in vivo. **B)** Schema of cell divisions in laser-ablated Neuromasts. 78% of sustentacular cell divisions demonstrate self-renewal, while 16% produce a pair of hair cells. In 3% of cases, they generate a pair of mantle cells, while in another 3%, one mantle cell and one sustentacular cell are generated. Cell divisions of mantle cells show complete self-renewal. **C)** Number of cells for each cell type as a function of time. Dots correspond to Experimental data from Viader-Llargués et al., 2018 (9) and continuous lines are model fit to experimental data. **D)** Growth rates of Sustentacular (blue) and Mantle (red) cells as a function of the number of cells corresponding to Eqs. S5 and S6. The maximal growth rates of sustentacular and mantle cells show a strong sigmoidal behaviour.

These results indicate that the response observed during neuromast regeneration can be explained in terms of a proliferative response of sustentacular and mantle cells that is cooperatively controlled by

each cell type. An important question is whether this cooperative control of cell proliferation is globally generated or achieved by local interactions between neighbouring cells.

2.2 2D cell-based model of the zebrafish neuromast: a stable initial condition

Because spatial relationship between cells is not considered in the ordinary differential equations-based model, we decided to develop a two-dimensional cell-based computational model. In particular, we opted for the Cellular Potts Model (CPM) formalism, which is lattice-based and allows realistic cellular shapes and dynamics (see Computational Methods section 4.2). This model is optimal because the neuromast is a complex non-stratified epithelium, whose cells divide largely within a single plane perpendicular to their apicobasal axis. We first modelled the uninjured neuromast as a two-dimensional disc of cells, respecting the empirical number of hair, sustentacular and mantle cells, as well as their spatial distribution. We parameterized the cell target areas and perimeters (see details in Computational Methods section 4.2) together with the corresponding Lagrange multipliers of the CPM Hamiltonian (Table S3) to reproduce in average the geometrical features of the neuromast cells (Fig. 2 top). Next, we asked under what conditions the architecture of the *in silico* neuromast is stable by exploring the Hamiltonian parameters accounting for the local binding energies ($J_{\alpha\beta}$) between cells and between a cell and its outside tissue (where α and β are either two neighbouring neuromast cells or a neuromast cell and the outside tissue). In particular, all the binding energies are J_{HH}, J_{SS}, J_{MM}, J_{HS}, J_{HM}, J_{SM}, J_{HO}, J_{SO} and J_{MO}, corresponding to the binding between hair cells, sustentacular cells, mantle cells, hair with sustentacular cells, hair with mantle cells, sustentacular with mantle cells, hair cells with the outside tissue, sustentacular cells with the outside tissue and mantle cells with the outside tissue, respectively.

We first excluded binding energies that, while maintaining the organ's circular shape, strongly reduced intercellular adhesion (Fig. 2A, Movie S1 and Table S4) and increased intercalation of sustentacular with hair and mantle cells (due to a high repulsion of cells of the same type, Fig. 2B, Movie S2 and Table S4). We eventually found a convenient parametrization satisfying a stable tissue (Fig. 2C, Movie S3 and Table S4). This stable configuration was achieved by i) repulsion of hair cells with mantle cells to ensure separation ($J_{HM} > 0$), ii) adhesion of sustentacular cells with both mantle ($J_{SM} < 0$) and hair cells ($J_{SH} < 0$), iii) repulsion of the outside tissue with the hair cells, which in turn was higher than the repulsion with the sustentacular cells ($J_{OH} > J_{OS} > 0$), and iv) adhesion of the supporting cells (sustentacular and mantle cells) higher than the adhesion of the hair cells, which in turn was higher than the homotypic adhesion of the hair cells ($J_{SS} < J_{SH} < J_{HH} < 0$, $J_{MM} < J_{SH} < J_{HH} < 0$, $J_{SM} < J_{SH} < J_{HH} < 0$), in agreement with the mechanical stresses of these cells recently estimated using ForSys (11) (Table S4).

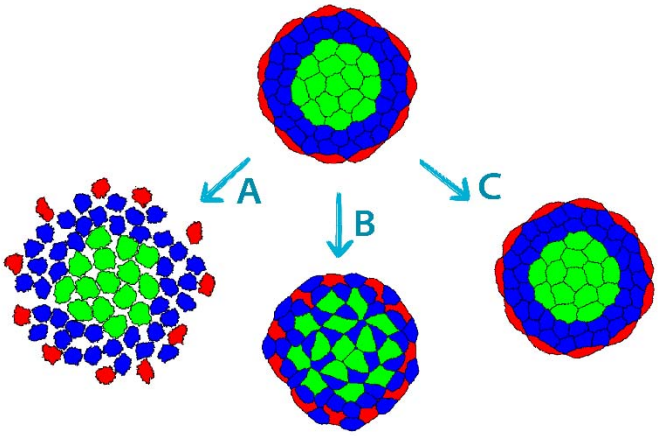

Figure 2. Tuning model binding energy parameters leads to a stable *in silico* neuromast. (A) Non appropriate CPM binding parameter values distort the initial tissue architectures leading to disintegration or (B) anomalous tissue architectures that show intercalation of the sustentacular, hair, and mantle cells. (C) A well-defined model parameter space region can maintain stable neuromasts (Movies S1-S3). Panels A, B and C show the simulated tissues after a simulation time of 30000 MCS (Monte Carlo steps) that correspond to 1 day post injury. Hair, sustentacular and mantle cells in green, blue and red, respectively. Energy binding parameter values depicted in Table S4 while the rest of the CPM parameters in Table S3.

2.3 Uncontrolled supporting cell proliferation in in the neuromast can drive unlimited neuromast growth *in silico*

It has been experimentally determined that following the loss of up to 90% of their cellular content (by laser ablating all but 4-10 cells), neuromasts regenerate by attaining radial symmetry within 3 days post-injury, and subsequently achieve a normal composition and proportions of cell types by 7 days post-injury (dpi). To recapitulate this natural response, we introduced cell divisions in the model. We modelled the cell fates of the sustentacular cell daughters satisfying Eq. 1, in the same spirit of the preliminary model presented section 2.1. (Table S1, (9)).

In neuromast, the position of the dividing cells correlates with the outcome of the regenerative process: sustentacular cells leading to one sustentacular and one mantle cell or two mantle cells consistently occur at the outer perimeter of the neuromast, whereas divisions generating hair cells are observed near the centre and self-renewing sustentacular cell divisions occupy the area between them (9). This indicates sustentacular cell fate decisions vary along the radial coordinate within the neuromast. This mediolateral correlation could reflect a signal originated at the centre of the organ or in the surrounding tissue diffusing radially out or in, respectively (see Discussion section). Thus, we modelled the dynamics of cell proliferation for the sustentacular cells by using a minimal radial potential constituted by a radial step function (Supp. Fig. S3 A). This allowed us to distinguish two

regions defined by a critical distance r_c with respect to the centre of mass of the neuromast. If the centre of a cell is located within a radius smaller than r_c, we will say it belongs to the central region; if it is located within a radius greater than r_c, we will say it is in the region we call peripheral. We assumed that mitoses of sustentacular cells whose centroids are within a certain critical distance r_c from the neuromast centre of masses would generate two sustentacular cells with probability p_{SS}^{c} or two hair cells with the previously reported proportion p_{HH}. Otherwise, the two daughter cells are both sustentacular with probability p_{SS}^{p}. In this periphery region, cell division can also lead to two mantle cells or one mantle and one sustentacular, where the probabilities of these two last cases are the already known probabilities p_{MM} and p_{SM} (see method). By construction, the probability of sustentacular cell divisions occurring within a circle of radius d_c (p_{SS}^{c}) and in the periphery (p_{SS}^{p}) are constrained to the known p_{SS} value above indicated in section 2.1 (Table S1).

We implemented cell division as follows. When a cell divides, a line with a random slope passing through the cellular centre of mass separates the mother cell in two, creating the future daughter cells in the next time step (Supp.Fig. S3 B i, ii and iii), the nodes of the mother cell on either side of this line are allocated to two daughter cells. Although the new-born cells have approximately half of the mother cell area, the Hamiltonian area term will drive an increase in size within a few simulation steps. We set the sustentacular cell division probability to be twice as fast as that of mantle cells (9), (Table S3).

With this parameterized cell proliferation, we conducted simulations of a stable neuromast (parameters detailed in Tables S3 and S4) consisting of 15 hair cells, 40 Sustentacular cells, and 11 mantle cells, from which all but 4-10 cells were removed, simulating the experimental ablation. Our findings indicate that the neuromast undergoes regeneration but continues to grow unabated (see Supp. Fig. S3 C and Movie S4). Unsurprisingly, the uninjured organ also grows (Supp. Fig. S3 D and Movie S5). Hence, although the model succeeds in initiating the regenerative response, it fails in slowing it down as experimentally observed. Thus, the model requires a control mechanism to regulate the proliferative response triggered by injury.

2.4 Feedback switch depending on the number of neighbouring cells can control ablation-derived cell proliferation in the *in silico* neuromast

We entertain the hypothesis that cell division in the neuromast is modulated locally by neighbouring cells. In particular, the division rate of each of the premitotic sustentacular and mantle cells could depend on the number of neighbouring cells N_{neigh}, regardless of their types. Hence, a switch mechanism may emerge from the local cellular neighbourhood and modulate the cellular division rate: whenever N_{neigh} exceeds a certain threshold represented by a parameter that we call "Proliferation switch" (*S*), the cell arrests in the cell cycle and therefore stops dividing. We implemented this mechanism and investigated the evolution of the neuromast after removing all but 4-10 cells *in silico*. This showed that the neuromast successfully engages in a strong but transient proliferative response. We found that the proliferation switch, which better describes the experimental data, occurs when cells acquire three identical neighbours. (Supp. Fig. S3 E and Movie S6). Nevertheless, although the model is in general capable of qualitatively regenerating the organ

after injury, the steady state tissue architecture of the regenerative neuromast contains more than triple the number of mantle cells than the initial tissue (Supp. Fig. S3 E and Movie S6).

2.5 Spatial heterogeneity of the feedback switch can qualitatively explain cell proliferation of supporting neuromast cells after injury

An important assumption underlying the previous model is the existence of a unique switch for all proliferating cells. We reasoned that this could be the reason for the model's failure to achieve the original architecture of the neuromast. Therefore, we formulated an alternative mechanism assuming that the cell division switch depends on the cell type *i.e.*, the number of cells upon which cell division of sustentacular cells (S_s) and mantle cells (S_m) should stop are not necessarily equal.

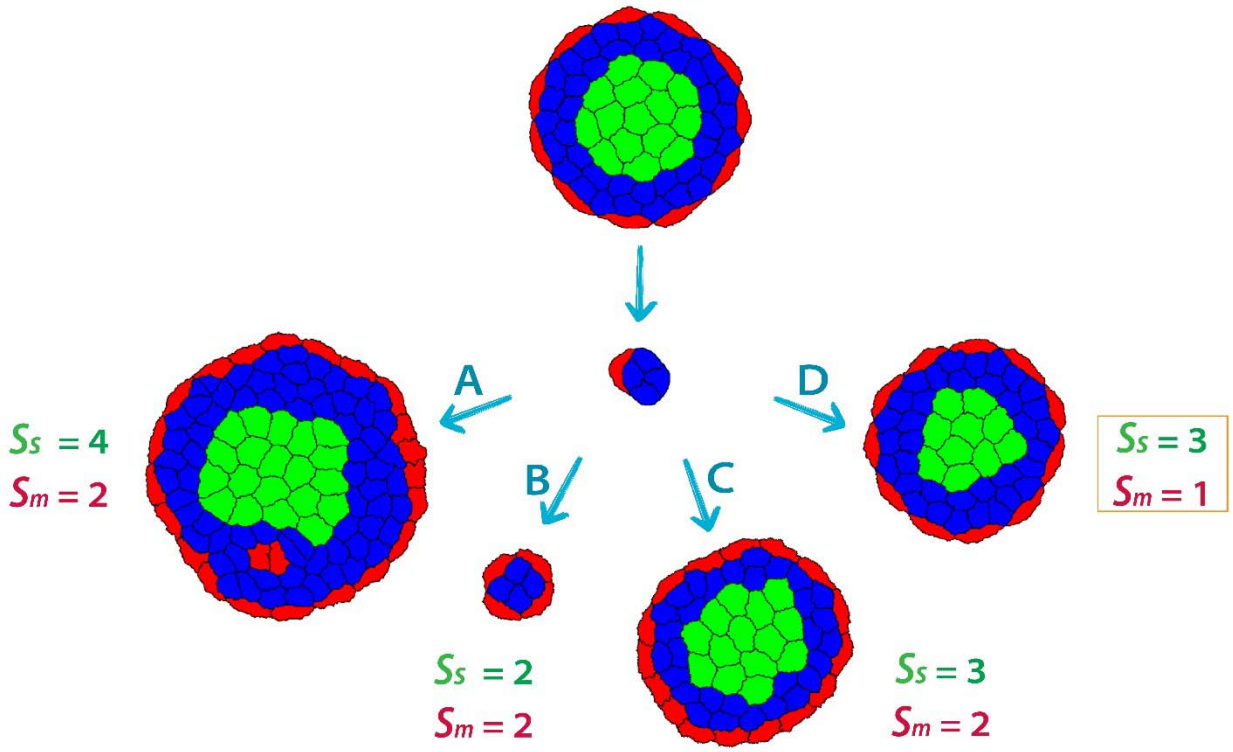

Figure 3. Tuning proliferation switch of sustentacular and mantle cells. (A-C) Simulation of an *in silico* neuromast subjected to an ablation in which all but 4-10 cells were removed and while the proliferation switch for mantle cells (S_m) was fixed in 2, the proliferation of sustentacular cells (S_s) was 4 (A), 2 (B) and 3 (C) **(D)** Simulation as in (A-C) but while the proliferation switch for sustentacular cells (S_m) was fixed in 3, the proliferation of mantle cells (S_s) was number 1. Panel A shows the simulated tissue after a simulation time of 90000 MCS corresponding to 3 days post injury. Panels B-D show the simulated tissues after a simulation time of 210000 MCS corresponding to 7 days post injury. Hair, sustentacular and mantle cells in green, blue and red, respectively. All remaining model parameter values depicted in Tables S3 and S4. Note that the central tissue depicts a representative neuromast ablated leaving between 4 to 10 remaining cells. (Complete simulations depicted in Movies S7-S10)

We tested this possibility by *in silico* ablating all but 4-10 cells of the neuromast and arbitrarily setting the cell division switch of mantle cells to $S_m = 2$. When the cell division switch of the sustentacular cells was $S_s = 4$, the ablation led to bigger and distorted neuromasts, with multiple clusters of hair cells and even transient clusters of mantle cells (Fig. 3A and Movie S7). In contrast, for S_s equal to two, tissue growing does not really take off upon ablation and the organ remains small lacking the central hair cluster (Fig. 3B and Movie S8). When setting S_s to three, the neuromast size and architecture begin to progress according to previously reported empirical data (Fig. 3C and Movie S9).

We next explored the cell division switch of mantle cells while fixing S_s to three. Since we had already explored S_m =2, which resulted in an excessive number of mantle cells (Fig. 3C and Movie S9), and considering that S_m =0 would imply no divisions at all, we decided to test S_m =1. This parametrization qualitatively recapitulates the previously reported regenerative response of the neuromast when ablating all but 4-10 cells (Fig. 3D and Movie S10)

2.6 Quantitative comparison of model simulations with experimental data indicates the existence of a delay between ablation and cell division burst.

To further investigate the closeness of the cell type-specific division switch to data from regenerating neuromasts, we challenged our model by comparing the predicted kinetics of total cell number and cell proportions of the simulations with the corresponding experimental data (9). Although the results show that there is qualitative agreement between model simulations and experimental curves, we observed a distinctive difference in both, the total cell number (Fig. 4A i) and the number of each cell type (Fig. 4 A ii-iv) of the regenerating neuromast, immediately after injury. This difference suggests that cell divisions are not immediately triggered after the ablation but after a certain delay. To test this possibility, we included an explicit delay in our model between the ablation time and the time in which cells start to proliferate, regardless of their cell type. Fitting this delay led us to conclude that the experimental data can be recapitulated when assuming a delay of 0.8 days (Fig. 4 B i'-iv'). Interestingly, this result is in agreement with the first wave of divisions previously observed (9) (see all model parameters in Tables S3 and S4).

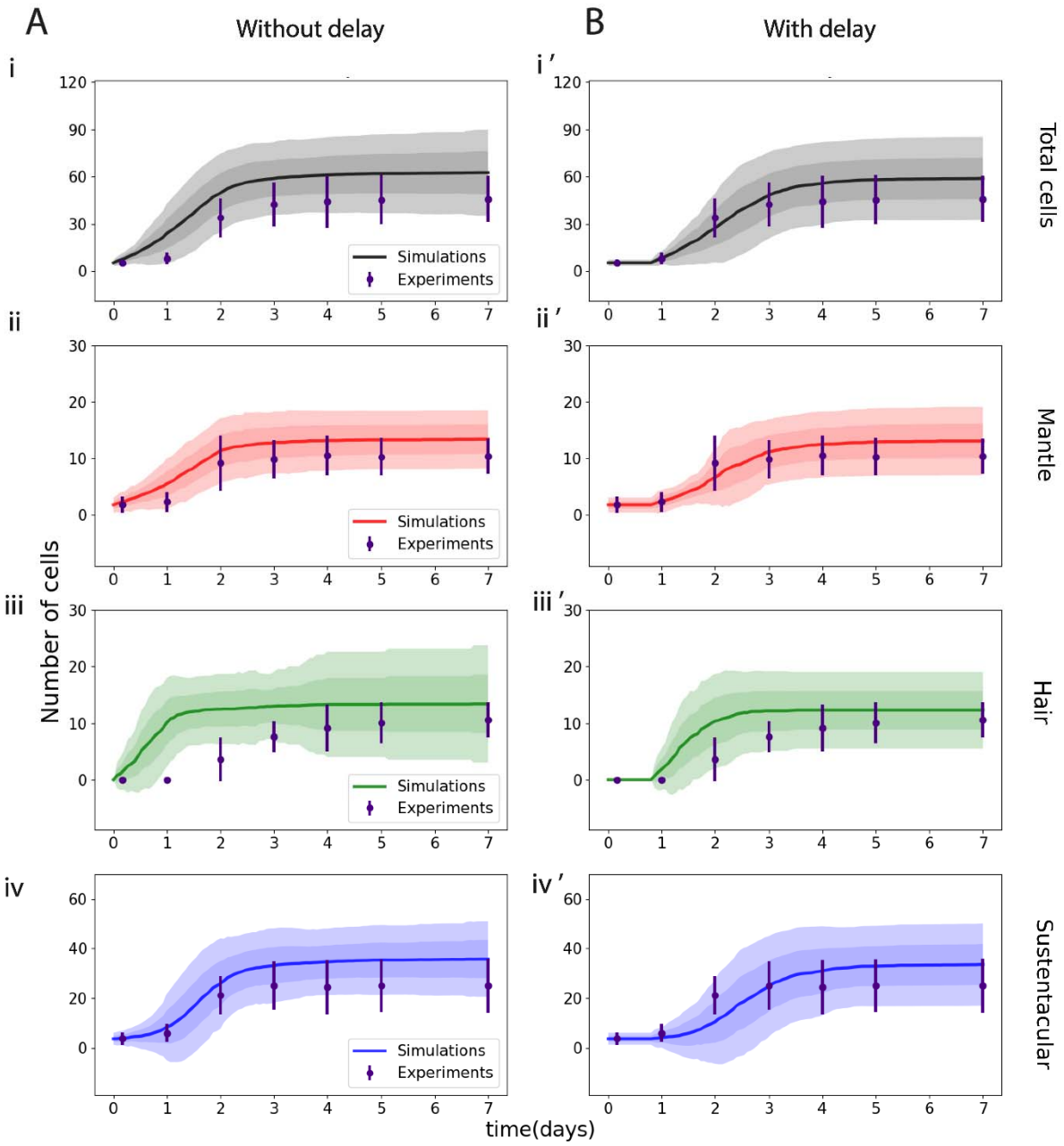

Figure 4. Quantitative comparison between model-predicted simulations and experimental data suggests the existence of a delay between the ablation and cell division burst. Predicted evolution of the neuromast cell numbers assuming that cells divide immediately after ablation **(A i, ii, iii, iv)** or after a delay of 0.8 days **(B i', ii', iii', iv')**. Time evolution of experimental and simulated neuromast total number of cells **(i, i')** and cell proportions **(ii, ii', iii, iii', iv, iv')** after an ablation of all but 4-10 cells. Cell proliferation switches are 3 for sustentacular cells and 1 for mantle cells. All model parameters depicted in Tables S3 and S4. Model simulations (with and without delay) correspond to 45 replicates obtained from 45 stochastic seeds and are

depicted as shaded areas, from lighter to darker, corresponding to the 68 % and 95 % confidence intervals, respectively. Points and error bars in each panel correspond to the experimental mean and two standard deviations obtained from 15 replicates reproduced from Viader-Llargués *et a*l., 2018 (9).

2.7 The switch on ablation-derived cell proliferation can give rise to isotropy in the neuromast regenerative response

Previous results showed that the ablation of the posterior half of the neuromast leads to a very clear regenerative response (9). When this ablation paradigm was implemented *in silico*, our modelled neuromast was able to regenerate isotopically like its experimental counterpart. (Fig. 5 A-B, Movie S11). Furthermore, simulations in which all mantle cells were ablated resulted in a completely regenerated neuromast (Fig. 5 C and D, Movie S12), as observed in the experiments (9). Hence, our simulations show that our model qualitatively reproduces the isotropic regenerative responses experimentally observed in the neuromast after two ablation paradigms.

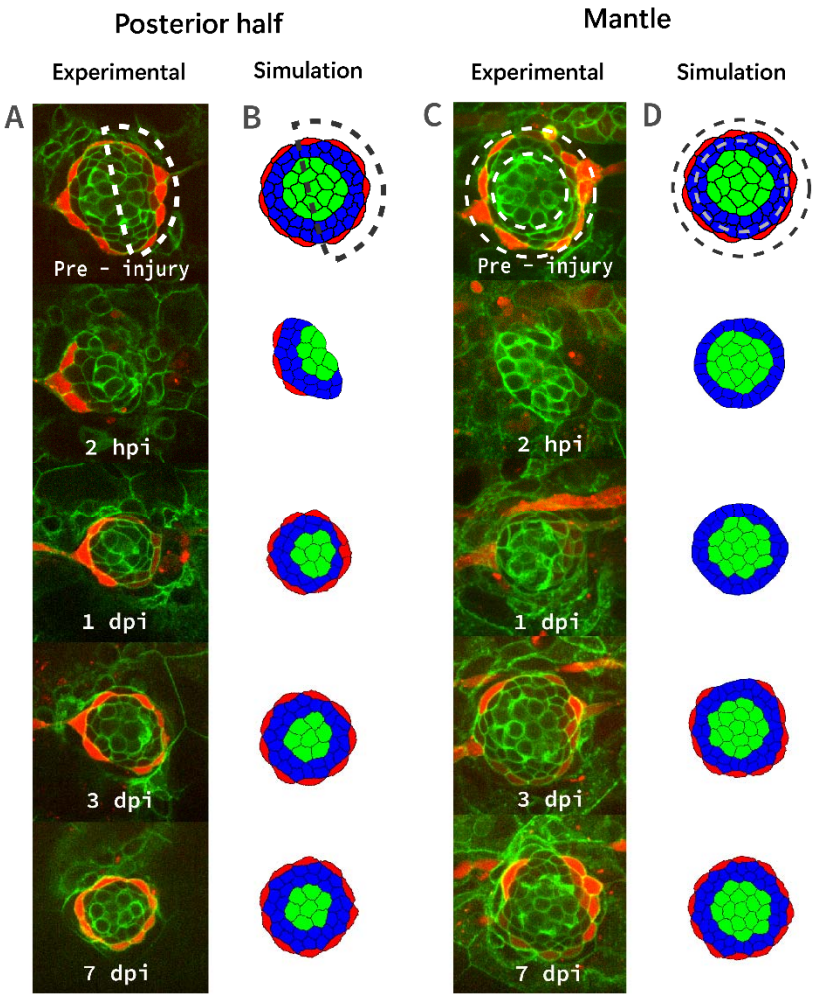

Figure 5. Isotropic regenerative responses of the model upon different *in silico* ablation paradigms recapitulate experimental neuromast progression during regeneration. Time evolution of experimental **(A, C)** and modelled **(B, D)** neuromasts subjected to posterior half (A, B) and mantel cells (C, D) ablation. From top to bottom, time corresponds to pre-injury, 2 hpi, 1 dpi, 3 dpi and 7 dpi in the experiments and to the initial condition, 2500, 30000, 90000 and 210000 MCS in the simulations (B, D). The two complete simulations are visualized in Movies S11 and S12. Cell proliferation switches as in Fig. 3 D. Hair, sustentacular and mantle cells in green, blue and red, respectively. CPM parameter values depicted in Tables S3 and S4. Experimental panels A and C show membrane cells in green (Cldnb:lynGFP marker) and mantle cells in red (Alpl:mCherry).

2.8 Model-predicted proliferation switches agree with experimental data on cell neighbourhood quantification

A crucial element of our model is that sustentacular and mantle cells stop proliferating when the number of neighbours of the same type reaches the corresponding switches. One would predict that sustentacular and mantle cells should have a number of sustentacular and mantle neighbours, respectively, similar to their proliferation switches. Thus, we decided to test this prediction experimentally, by ablating all but 4-10 cells in the neuromasts of zebrafish larvae and detecting the number of neighbouring cells of each dividing cell. Since the regenerative response observed after ablation shows that the number of cells converges to a plateau in approximately 3 days post ablation (Fig. 4), we evaluated these predictions during this time. We ablated cells in larval neuromasts, imaged and segmented the tissue after 3 days, and retrospectively determined cell fate after cell division to identify sustentacular and mantle cells and their neighbours 30 min before each mitosis (Fig. 6 A-E, Supp. Fig. S6, Movie S13, see section 4.2 for details). In parallel, we performed simulations with our model recreating the ablation of all but 4-10 cells scenario (Fig. 6 A'-D'), counted the number of neighbours of each cell type accumulated during 3 days post ablation and compared it with the experimental data. Despite the higher scatter of the experimental data, the results show that at 3 days post ablation, the number of sustentacular cells neighbouring sustentacular cells (and the same for mantle cells) predicted by the model overlaps with that observed experimentally. (Fig. 6 F, G). These results further support the hypothesis that the proliferation of both mantle and sustentacular cells can be modulated by a local mechanism depending on the specific number of neighbouring cells.

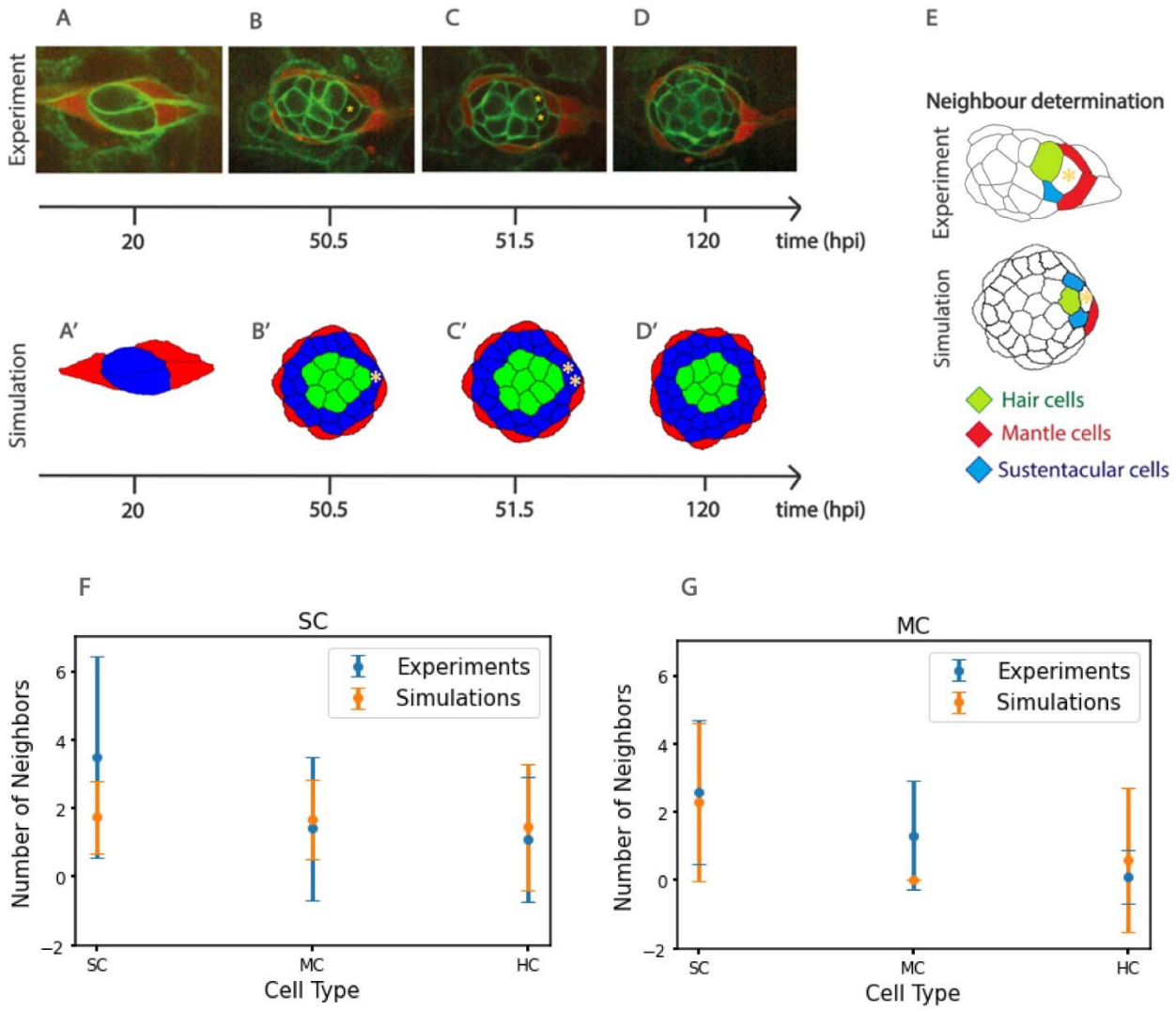

Figure 6. Quantitative comparison between experimentally determined and model-predicted simulations of the cell neighbours of neuromast cells before division. **(A, B, C, D)** Microscopy images depicting the temporal evolution of an ablated neuromast, where the moment of sustentacular cell division is identified. **(A', B', C', D')** Simulation with our model replicating the experiment. **(E)** Schematic illustrating the type and number of neighbours of the sustentacular cell undergoing division (experiment above, simulation below). **(F, G)** Quantification of number of cell neighbours of sustentacular and mantle cells experimentally determined (C) and predicted by the computational model (D). *n* = 8 fish.

3. Discussion

Regeneration is a tissue-scale process that channels individual cells to collectively respond to damage to rebuild an organ. In vertebrates, when the damage is severe the prevailing regenerative mechanism involves the controlled execution of cellular proliferation (12,13). Although mitotic cell divisions are essential to replenish cell numbers, they must be tightly regulated to prevent organ hyperplasia and proportional imbalance. The neuromasts are ideally suited to construct a predictive model of regeneration because they have a well conserved size and proportions, which invariably recover during regeneration. Importantly, neuromast regeneration occurs by epimorphosis, during which the sustentacular cells that remain after injury proliferate without de-differentiating or the formation of a blastema. Moreover, neuromast-size control is a purely local process that occurs independently of functional demand or systemic signals.

Despite the anatomical simplicity of the neuromast, modelling the regeneration of a complete organ presents various challenges. Chiefly among them is the need to integrate the cellular and supra-cellular dynamics of non-identical cells. Therefore, to simulate the spatiotemporal dynamics of cells in the neuromast we chose a Cellular Potts Model (CPM) (14). We found that a stable neuromast configuration emerges from a particular distribution of homo- and heterotypic adhesions and repulsions involving the hair cells and supporting cells, parameterized from previous mechanical inference performed using ForSys (11). We could reproduce *in silico* the changes in cell numbers when introducing a 24-hour delay in the proliferative response to injury (Fig. 4). Remarkably, this agrees with the experimentally-observed lag between injury and the first round of divisions of the sustentacular cell population (9).

It has been previously reported that the mitogenic activity of Wnt signaling induces sustentacular cells division in neuromasts, and that the Wnt-inhibitor Dkk limits further sustentacular-cell divisions when regenerating hair cells reach a certain threshold (30). We reasoned that if sustentacular cells would cease proliferation by local contact with Dkk-expressing hair cells, only the sustentacular cells that are immediately adjacent to hair cells would stop proliferating, whereas more distant sustentacular cells would continue dividing. Yet, we did not see such asymmetric pattern of cell division along the mediolateral axis of the neuromast, indicating that Dkk blocks sustentacular-cell divisions equally across the tissue, or that proliferation control via Wnt occurs independently of hair cells. Therefore, in follow-up studies it would be interesting to determine sustentacular-cell numbers in neuromasts chronically lacking hair cells.

We also explored an intriguing hypothesis: that the number of neighbouring cells of the same type control proliferation. This would be akin to cell-type specific local quorum sensing. By comparing model simulations with experimental data, we found that neuromast regeneration in zebrafish is consistent with sustentacular and mantle cells stopping proliferation when surrounded by three neighbouring sustentacular cells and between zero and two neighbouring mantle cells, respectively. Interestingly, this hypothetical mechanism of proliferation control not only induces local maintenance of cell proportions, but also results in an emergent control of organ size. Although the precise mechanism by which cell proliferation is halted during neuromast regeneration is beyond the scope of the present study, it can be speculated that it may ultimately result from mechanical cues and cell density, as has been observed during mouse utricle development (15). Notably, our hypothetical

mechanism of local control is consistent with the proposed 'neighbourhood watch' model, in which cells make decisions based only on communication with their local environment when they detect variations in signal intensity relative to their neighbours (16).

A corollary of our computational model is that, on average, the sustentacular and the mantle cells should divide until they number of their neighbouring sustentacular and mantle cells is three and between zero and two, respectively. These predictions agreed with our experimentally determined quantification of cell neighbours (Fig. 6).

Therefore, we conclude that neuromast regeneration follows a delayed onset of cellular proliferation coupled with negative feedback triggered by the cells' immediate neighbourhood. This mode or growth control that propagates as the tissue grows may be more general than previously recognized. More generally, our approach combining a computer model parameterized with empirical data can make unconventional predictions and guide experimental tests.

4.1 Computational methods section

4.1.1 Non-spatial mathematical model of the neuromast cell number kinetics

We developed a mathematical model describing the time course of cell number of each cell type responsible for the regenerative response observed in the zebrafish neuromast. The main variables of the model are the time post ablation (*t*), the number of hair (*H*), mantle (*M*) and sustentacular (*S*) cells. The rich diversity of sustentacular cells progeny was encoded in the probabilities by which a sustentacular cell could give rise to sustentacular cells (p_{SS}), mantle cells (p_{MM}), hair cells (p_{HH}) or mantle and sustentacular cells (p_{SM}), as previously reported (Table S1). Thus, sustentacular cells can be generated by sustentacular cells in symmetric or asymmetric cell divisions as follows:

$$\frac{dS}{dt} = (p_{SS} - p_{MM} - p_{HH})\nu_S(S)S \qquad \text{(Eq. S1)}$$

Because of Eq. 1 of the main text, we can rewrite this expression as:

$$\frac{dS}{dt} = (2p_{SS} + p_{SM} - 1)\nu_S(S)S \qquad \text{(Eq. S2)}$$

Where ν_S is the proliferation rate of sustentacular cells. We also assumed that mantle cells only render mantle cells after cell divisions and can be generated out of symmetric or asymmetric divisions of sustentacular cells or symmetric divisions of mantle cells as follows:

$$\frac{dM}{dt} = (2p_{MM} + p_{SM})\nu_S(S)S + \nu_M(M)M \qquad \text{(Eq. S3)}$$

Where ν_M is the proliferation rate of mantle cells. Based on previous results (9), we assumed that hair cells do not divide but can be generated symmetrically by sustentacular cells (with probability $p_{HH} = 1 - p_{SS} - p_{MM} - p_{SM}$):

$$\frac{dH}{dt} = 2(1 - p_{SS} - p_{MM} - p_{SM})\nu_S(S)S \qquad \text{(Eq. S4)}$$

We assumed that the proliferative response of both sustentacular and mantle cells is controlled and we assumed a Hill-expression as follows:

$$\nu_S(S) = \frac{\nu S_{50}^h}{S_{50}^h + S^h} \quad \text{(Eq. S5)}$$

$$\nu_M(M) = \frac{f\nu M_{50}^h}{M_{50}^h + M^h} \quad \text{(Eq. S6)}$$

The parameters of this expression are the number of sustentacular (mantle) cells to render 50 % of the maximal proliferative response, which was ν ($f\nu$) for sustentacular (mantle) cells and h, the Hill-exponent typically denoting certain cooperativity (17), which for the sake of simplicity was assumed unique for both cell types. With these expressions, the model is given by the following ODEs system:

$$\frac{dS}{dt} = (2p_{SS} + p_{SM} - 1)\frac{\nu S_{50}^h S}{S_{50}^h + S^h} \quad \text{(Eq. S7)}$$

$$\frac{dM}{dt} = (2p_{MM} + p_{SM})\frac{\nu S_{50}^h S}{S_{50}^h + S^h} + \frac{f\nu M_{50}^h M}{M_{50}^h + M^h} \quad \text{(Eq. S8)}$$

$$\frac{dH}{dt} = 2(1 - p_{SS} - p_{MM} - p_{SM})\frac{\nu S_{50}^h S}{S_{50}^h + S^h} \quad \text{(Eq. S9)}$$

4.1.2 Numerical Solution of the non-spatial mathematical model of the neuromast cell number kinetics

The mathematical model, comprising the system of ordinary differential equations (ODEs) as outlined in Eqs. S7, S8 and S9, was numerically solved to study the dynamics of the neuromast cell types in zebrafish.

The complete analysis was conducted within a Jupyter Notebook (18) using Python version 3.11 (19) as kernel. Specifically, the numerical integration of the ODEs was performed using the odeint (20) function from the scipy.integrate module in the SciPy library (21) . Parameter estimation was carried out using the Python package pyabc (22) (Supp. Fig. S1), which implements Approximate Bayesian Computation (ABC) methods for model fitting. For the analysis and visualization of the data, parameter distributions and model predictions we employed Pandas (23), Numpy (24), Matplotlib (25) and Seaborn (26).

The Jupyter Notebook, which details the step-by-step implementation of the ODEs model presented in Results section 2.1 and the corresponding analysis, is available in this GitHub repository: https://github.com/ecuracosta/diff_eq_zebrafish (27).

4.1.3 Spatial Computational cell-based model of the regenerating neuromast after laser ablation

We implemented a two-dimensional Cellular Potts Model(CPM) (28,29) in Morpheus (30). In this formalism, individual cells are represented as sets of sites on a discrete lattice, which in our case is a 2D grid. Each site on the lattice is identified by its position *ij* where *i* is the row and *j* the column, each cell is represented with an "ID" number (denoted as σ) and the "type" of cell it belongs to (identified by the letter τ). The ID is a unique number that identifies each cell, while the type is a label that defines the properties and characteristics of the cell, therefore, two cells have different σ but can share the same τ if they are of the same type.

In the Cellular Potts Model (CPM), when representing a system containing a total of *n* cells, each site *ij* in the lattice with the same σ , for example σ = *M* (where *M* ranges from 1 to *n*) corresponds to the cell labeled as *M*. Moreover, σ equal to 0 is utilized to denote the medium surrounding the cells.

The energy of any given cell configuration is determined by an energy function or Hamiltonian defined as follows:

$$H\left(J_p, \lambda_p, P, \lambda_a, A\right) = \sum_{ij} J_{\tau(\sigma_{ij})\tau(\sigma_{i'j'})}(1 - \delta_{\sigma_{ij},\sigma_{i'j'}}) + \sum_{\sigma} \lambda_p (p_\sigma - P_{T(\tau(\sigma))})^2 + \sum_{\sigma} \lambda_a (a_\sigma - A_{T(\tau(\sigma))})^2$$

(Eq. S10)

Where $J_{\tau(\sigma_{ij})\tau(\sigma_{i'j'})}$ is the coupling coefficient that determines the adhesion between site ij and its selected neighboring site *i'j'*, δ is the Kronecker delta and the second and third terms represent the energies associated with cell area elasticity and perimeter contractions, respectively, and include the Lagrange multipliers λ_a (elasticity coefficient) and λ_p (contractibility coefficient). "a" and "p" represent the area and perimeter of the cell σ, respectively, while "A_T" and "P_T" are the target area and perimeter, respectively.

The model's evolution is based on the Metropolis algorithm (31,32), which involves randomly selecting a site on the lattice and evaluating whether changing the cell's identity at that site would decrease the system's energy. If the change results in a decrease in energy, it is accepted deterministically; otherwise, it is accepted with a probability based on the Boltzmann distribution, introducing a stochastic component. The system's energy function (*H*) accounts for the interactions between neighbouring cells, their properties, and preferences for certain locations on the lattice. This energy function influences the stability and behaviour of cells in the tissue.

We incorporated cell division into our CPM as a probabilistic process, where at each time step, for each cell with the potential to divide (*i.e.*, Sustentacular and Mantle cells), we randomly draw a number between zero and one from uniform distribution. If this number is less than a parameter, we refer to as P_S for Sustentacular cells and P_M for Mantle cells (Table S3), the cell undergoes division.

As described in Section 2.3, we defined a radial potential that determines two regions. To achieve this, we constructed a function 'r' that represents the distance from the centre of a cell to the centre of the neuromast, which we defined for each cell as:

$$r = \sqrt[2]{(x_i - X)^2 + (y_i - Y)^2} \qquad \text{(Eq. S11)}$$

- x_i = the 'x' coordinate of the cell's center
- X = the 'x' coordinate of the neuromast's centre of mass
- y_i = the 'y' coordinate of the cell's center
- Y = the 'y' coordinate of the neuromast's centre of mass

Using this function, we established two regions: the central and peripheral regions, defined as $r < d_c$ and $r \geq d_c$, respectively, where 'd_c' is a scalar representing the critical distance from which we modelled cell differentiation (see Section 2.3).

The decisions regarding cell fate vary along the radial coordinate. To model the cell fate decisions of a sustentacular cell along the radial coordinate, we decided to distribute the experimentally found probabilities (Eq. 1) into these two regions (central and peripheral). We arranged it in such a way that the total divisions resulting in two hair cells occur in the central region, the total divisions resulting in mantle cells in their progeny occur in the peripheral region, and those resulting in two sustentacular cells may occur in both regions. As cell fate implementation is stochastic in our model, we constructed two probability equations, one for each region, central and periphery respectively:

$$P_{SS}{}^{c} + P_{HH} = 1 \qquad \text{(Eq. S12)}$$

$$P_{SS}{}^{p} + P_{MM} + P_{SM} = 1 \qquad \text{(Eq. S13)}$$

4.1.4 Spatial cell-based model implementation and parametrization

We implemented our computational model by using Morpheus, version 2.2.6 (30). To estimate the target areas (A_T) and target perimeters (P_T) for each cell class, we utilized five epifluorescence microscopy images at final time from independent neuromast ablation experiments. Using Fiji (33), we converted the images to grayscale. Subsequently, we employed Morpheus software (30) to obtain the areas and perimeters of each cell, using a grid of the same dimensions as the microscopy image, with an equivalence of 1px = 0.102 micrometres = 1 lattice node. We used the averages of the area and perimeter of all cells of the same class present in all images as our A_T and P_T values (Table S3).

To parameterize time, we conducted various simulations by increasing the number of Monte Carlo Steps (MCS) equivalent to one day until we found the value at which the proper tissue convergence is

ensured. We found that the optimal simulation time corresponds to 30,000 MCS, equivalent to one day.

We explored different values of d_c and we found that values less than 80 and greater than 100 generate hypotrophy and hypertrophy in the number of hair cells, respectively. Therefore, we decide to analyse five different values of d_c between 80 to 100: 80, 85, 90, 95, and 100 nodes, equivalent to 8.16, 8.67, 9.18, 9.69, and 10.2 micrometres, respectively. For each one, we performed 30 simulations starting with 4-10 cells and compared the average final number of cells of each type with the average values from 15 experiments obtained from Viader-Llaguer et al (9). The optimal value of "d_c" that we obtained was 95 nodes = 9.69 micrometres.

For the P_S and P_M parameters of our model, we decided to maintain the relationship reported in Viader-Llargués et al., 2018 (9), where P_S = 3/2 P_M (Table S3).

To parameterize the type of progeny of a Sustentacular cell according to the region in which it is located, we relate the probabilities of a division being of type SS, SH, SM, or MM (Eq.1) to those defined in equations S12 and S13, such that a percentage of the total SS divisions measured experimentally occur in the peripheral region and the rest in the central region. We studied two possible scenarios: that 60% of SS divisions occur in the peripheral region and 40% in the central region, and that 70% occur in the peripheral region and 30% in the central region. We conducted 45 simulations for each proposed scenario. Cases where the probability of SS in the central region were less than 30% and greater than 40% were discarded as they did not reproduce the experimentally observed phenomenology. This is because our model considers neighbours of the same class as a stopping mechanism, and if SS divisions occur with a high percentage, the mechanism is activated, impeding the regeneration process of the neuromast. Conversely, if the percentage is too low, in the initial divisions, all hair cells will be generated, leading to neuromast atrophy. To determine the appropriate parameterization, we compared the average number of cells of each class in the experimental final state with the simulated values. We found that the values that best reproduced the experiments involved assigning 70% of SS divisions to the peripheral region and 30% to the central region.

78% of the total divisions of a sustentacular cell during the regeneration process correspond to SS (see section 2.1 and Figure 1B). Consequently, 70% of these (54.6%) were assigned to the peripheral region, while the remaining 23.4% were designated to the central region. The rest of the percentages stay equal (HH 16%, SM 3%, MM 3%) and are allocated to their respective regions (see 4.1). In this manner, we can derive the probabilities ${P_{SS}}^c, P_{HH}, {P_{SS}}^p, P_{MM}, P_{SM}$.

For the central region we have 23.4 (%SS) + 16 (%HH) = 39.4. This calculation results in ${P_{SS}}^c = 0.594 \ and \ P_{HH} = 0.406$. In the same way, we calculated the probabilities in the peripheral region: ${P_{SS}}^p = 0.901$, $P_{MM} = 0.0495$ and $P_{SM} = 0.0495$.

The simulations corresponding to the 8 experiments, in which the number of neighbouring cells of neuromast cells before cell division is counted (Section 2.8), were generated with the initial condition being reconstructed from the first microscopy image taken after laser ablation in each experiment. Since the tissue is inflamed after ablation, the size of the cells in this condition is slightly bigger than the target area. To ensure that the temporal evolution from the initial condition to the target area is not

abrupt, we decided to define the Lagrange multiplier associated with the area as a sigmoidal function of time (Table S3).

Using the cell count data over time and a Python script developed for this purpose, we identified instances of cell division and recorded the number of neighbours of the same class that the cell had at the moment just before division.

The Morpheus-based model implementations presented in Results section 2.2-2.8 and the Python-based corresponding analysis is available in zenodo: https://zenodo.org/records/13922477 (34).

4.2 Experimental methods

4.2.1 Fish maintenance and breeding

Adult zebrafish were kept in standard conditions: 27.5ºC and a light/dark cycle of 14 and 10 hours. Double transgenic fish Tg(-8.0cldnb:LY-EGFP); Tg(myo6b:actb1-EGFP) were crossed with Tg(alpl:mCherry) fish. The progeny can be screened as soon as 24hpf by looking at green fluorescence in the heart and the epidermis. 50% of these double transgenic fish are alpl:mCherry positive too, and are screened by looking for red fluorescence at the retina.

4.2.2. UV Laser cell ablations

Cell ablations were performed as previously described(9,35). 3 dpf triple transgenic larvae were anesthetized and mounted laterally on their left side in 0.8% low-melting point agarose. Either the L2 or L3 neuromast was ablated by targeting all but 5-10 cells. The fish were released from the agarose and left to rest for at least 2 hours after treatment in fresh E3 medium without anaesthetic.

4.2.3 Long term videomicroscopy imaging.

After the rest period, the most active larvae were put in a 1:40 diluted tricaine solution and screened for nicks in the fins or tail that could signal some damage during previous manipulations. Selected fish were mounted in 0.8% agarose containing 1:40 tricaine stock solution, and covered in the same amount of anaesthetic in E3 medium after agarose solidified. Fish were imaged with a 63X water immersion objective with Zeiss Immersol W oil for up to three days. Frames were acquired serially in the green and red channels every 15 minutes. Each frame consists of a z-stack centred on the cell bodies with 6 slices above and 6 slices below, each slice separated by $1\mu m$. E3 medium was replaced every 12 hours with fresh medium with anaesthetic.

4.2.4 Image analysis

The time lapse videos were screened manually for dividing cells. For every frame where a mitotic cell was identified, the frame -2 (30 minutes before) was selected for segmentation with EpySeg (36). This segmentation was used to count and identify the cells in contact with the cell about to divide (Supp. Fig. S6). The cell type of each neighbour was visually annotated based on morphology; the presence or absence of red fluorescence; and the presence or absence of a hair cell cuticle (marked by myo6b:act 1b-EGFP) both in the segmented frame and throughout the movie.

Acknowledgements

The authors thank Prof. Dr. Tomás S. Grigera and all the members of the Chara laboratory for valuable comments and suggestions. N.G.L was funded by Doctoral fellowships from Agencia Nacional de Promoción Científica y Tecnológica of Argentina and CONICET, Argentina. J.R.M.-R. was funded by the European Union's Horizon 2020 research and innovation program under the HORIZON EUROPE Marie Sklodowska-Curie Actions grant agreement 840834. E.C.C was funded by a Postdoctoral fellowship from Agencia Nacional de Promoción Científica y Tecnológica of Argentina. A.B. was funded by the BMBF 01GQ1904 grant. HL-S received funding from the New York University Abu Dhabi. O.C. was funded by grants PICT-2017-2307 and PICT-2019-03828 from the Agencia Nacional de Promoción Científica y Tecnológica of Argentina and by a Biotechnology and Biological Sciences Research Council grant (grant number BB/X014908/1).

Author contributions

N.G.L implemented and simulated the Cellular Potts Models and analysed the in silico data. J.R.M.-R., A.B. and O.V.-L. acquired the zebrafish microscopy images and analysed the corresponding results. E.C.C. implemented and simulated the ODEs model. H.L.S. supervised the Zebrafish experiments and edited the manuscript. O.C. conceived the project, analysed the results, secured funding, supervised N.G.L, E.C.C., and A.B., and, finally, wrote the manuscript with contributions of all the authors.

References

1. Trembley A. Mémoires pour servir à l'histoire d'un genre de ploypes d'eau douce, à bras en forme de cornes. Durand; 1744. 388 p.

2. Bode HR. Head regeneration in Hydra. Dev Dyn. 2003;226(2):225–36.

3. Bosch TCG, Anton-Erxleben F, Hemmrich G, Khalturin K. The Hydra polyp: Nothing but an active stem cell community. Dev Growth Differ. 2010;52(1):15–25.

4. Aboobaker AA. Planarian stem cells: a simple paradigm for regeneration. Trends Cell Biol. 2011 May;21(5):304–11.

5. Ivankovic M, Haneckova R, Thommen A, Grohme MA, Vila-Farré M, Werner S, et al. Model systems for regeneration: planarians. Dev Camb Engl. 2019 Sep 11;146(17):dev167684.

6. Morrison JI, Lööf S, He P, Simon A. Salamander limb regeneration involves the activation of a multipotent skeletal muscle satellite cell population. J Cell Biol. 2006 Jan 30;172(3):433–40.

7. Cura Costa E, Otsuki L, Rodrigo Albors A, Tanaka EM, Chara O. Spatiotemporal control of cell cycle acceleration during axolotl spinal cord regeneration. Sánchez Alvarado A, Bronner ME, Marr C, editors. eLife. 2021 May 14;10:e55665.

8. Uemoto T, Abe G, Tamura K. Regrowth of zebrafish caudal fin regeneration is determined by the amputated length. Sci Rep. 2020 Jan 20;10(1):649.

9. Viader-Llargués O, Lupperger V, Pola-Morell L, Marr C, López-Schier H. Live cell-lineage tracing and machine learning reveal patterns of organ regeneration. Whitfield TT, editor. eLife. 2018 Mar 29;7:e30823.

10. Chickarmane V, Roeder AHK, Tarr PT, Cunha A, Tobin C, Meyerowitz EM. Computational Morphodynamics: A Modeling Framework to Understand Plant Growth. Annu Rev Plant Biol. 2010 Mar 11;61(Volume 61, 2010):65–87.

11. Borges A, Miranda-Rodríguez JR, Ceccarelli AS, Ventura G, Sedzinski J, López-Schier H, et al. ForSys: non-invasive stress inference from time-lapse microscopy [Internet]. bioRxiv; 2024 [cited 2024 Sep 10]. p. 2024.05.28.595800. Available from: https://www.biorxiv.org/content/10.1101/2024.05.28.595800v1

12. Tanaka EM. The Molecular and Cellular Choreography of Appendage Regeneration. Cell. 2016 Jun 16;165(7):1598–608.

13. Becker T, Becker CG. Regenerative neurogenesis: the integration of developmental, physiological and immune signals. Development. 2022 May 3;149(8):dev199907.

14. Voss-Böhme A. Multi-Scale Modeling in Morphogenesis: A Critical Analysis of the Cellular Potts Model. PLOS ONE. 2012 Sep 11;7(9):e42852.

15. Gnedeva K, Jacobo A, Salvi JD, Petelski AA, Hudspeth AJ. Elastic force restricts growth of the murine utricle. Whitfield TT, editor. eLife. 2017 Jul 25;6:e25681.

16. Lee HC, Hastings C, Oliveira NMM, Pérez-Carrasco R, Page KM, Wolpert L, et al. ‘Neighbourhood watch’ model: embryonic epiblast cells assess positional information in relation to their neighbours. Development. 2022 May 16;149(10):dev200295.

17. Cattoni DI, Chara O, Kaufman SB, Flecha FLG. Cooperativity in Binding Processes: New Insights from Phenomenological Modeling. PLOS ONE. 2015 Dec 30;10(12):e0146043.

18. Kluyver T, Ragan-Kelley B, Pérez F, Granger B, Bussonnier M, Frederic J, et al. Jupyter Notebooks—a publishing format for reproducible computational workflows [Internet]. IOS Press. 2016 [cited 2024 Apr 30]. Available from: https://ui.adsabs.harvard.edu/abs/2016ppap.book...87K

19. Python.org [Internet]. [cited 2024 Apr 30]. Python Release Python 3.11.0. Available from: https://www.python.org/downloads/release/python-3110/

20. Mulansky M, Ahnert K. Odeint library. Scholarpedia. 2014 Dec 27;9(12):32342.

21. Virtanen P, Gommers R, Oliphant TE, Haberland M, Reddy T, Cournapeau D, et al. SciPy 1.0: fundamental algorithms for scientific computing in Python. Nat Methods. 2020 Mar;17(3):261–72.

22. Schälte Y, Klinger E, Alamoudi E, Hasenauer J. pyABC: Efficient and robust easy-to-use approximate Bayesian computation. J Open Source Softw. 2022 Jun 25;7(74):4304.

23. McKinney W. Data Structures for Statistical Computing in Python. In 2010. p. 56–61.

24. Harris CR, Millman KJ, van der Walt SJ, Gommers R, Virtanen P, Cournapeau D, et al. Array programming with NumPy. Nature. 2020 Sep;585(7825):357–62.

25. Hunter JD. Matplotlib: A 2D Graphics Environment. Comput Sci Eng. 2007 May;9(3):90–5.

26. Waskom ML. seaborn: statistical data visualization. J Open Source Softw. 2021 Apr 6;6(60):3021.

27. Costa EC, Chara O. Differential equations notebooks for: Local control of cellular proliferation underlies neuromast regeneration in zebrafish. 2024 Oct 7 [cited 2024 Oct 18]; Available from: https://zenodo.org/records/13897106

28. Glazier JA, Graner F. Simulation of the differential adhesion driven rearrangement of biological cells. Phys Rev E. 1993 Mar 1;47(3):2128–54.

29. Graner F, Glazier JA. Simulation of biological cell sorting using a two-dimensional extended Potts model. Phys Rev Lett. 1992 Sep 28;69(13):2013–6.

30. Starruß J, de Back W, Brusch L, Deutsch A. Morpheus: a user-friendly modeling environment for multiscale and multicellular systems biology. Bioinforma Oxf Engl. 2014 May 1;30(9):1331–2.

31. Metropolis N, Rosenbluth AW, Rosenbluth MN, Teller AH, Teller E. Equation of State Calculations by Fast Computing Machines. J Chem Phys. 1953 Jun 1;21(6):1087–92.

32. Hastings WK. Monte Carlo Sampling Methods Using Markov Chains and Their Applications. Biometrika. 1970;57(1):97–109.

33. Schindelin J, Arganda-Carreras I, Frise E, Kaynig V, Longair M, Pietzsch T, et al. Fiji: an open-source platform for biological-image analysis. Nat Methods. 2012 Jun 28;9(7):676–82.

34. Lavalle NG, Chara O. Data and Code for Simulations and Analysis for: Local control of cellular proliferation underlies neuromast regeneration in zebrafish. 2024 Oct 18 [cited 2024 Oct 18]; Available from: https://zenodo.org/records/13922477

35. Xiao Y, Faucherre A, Pola-Morell L, Heddleston JM, Liu TL, Chew TL, et al. High-resolution live imaging reveals axon-glia interactions during peripheral nerve injury and repair in zebrafish. Dis Model Mech. 2015 Jun 1;8(6):553–64.

36. Aigouy B, Cortes C, Liu S, Prud'Homme B. EPySeg: a coding-free solution for automated segmentation of epithelia using deep learning. Dev Camb Engl. 2020 Dec 23;147(24):dev194589.

Supplementary Tables

Probability	Value
p_{MM}	0.3
p_{SS}	0.78
p_{SM}	0.3
p_{HH}	0.16

Table S1. Probabilities of self-renewal and differentiation of sustentacular cells.

Parameter	Value
M50	6.04 ± 0.04
S50	21.77 ± 0.15
h	34.18 ± 2.65
□	1.12 ± 0.00

Table S2. Parameters of non-spatial mathematical model (Section 4.1).

Parameter	Value
Initial number of Mantle	11
Initial number of Sustentacular	39
Initial number of Hair	15
λ_a *(Mantle)*	$\frac{time^2}{(1000^2 + time^2)}$
A_T*(Mantle)*	1643
λ_p *(Mantle)*	1
P_T*(Mantle)*	213

λ_a *(Sustentacular)*	$\frac{time^2}{(1000^2 + time^2)}$
A_T*(Sustentacular)*	1579
λ_p *(Sustentacular)*	1
P_T*(Sustentacular)*	177
λ_a *(Hair)*	$\frac{time^2}{(1000^2 + time^2)}$
A_T*(Hair)*	2597
λ_p*(Hair)*	1
P_T*(Hair)*	206
P_S	0.00015
P_M	0.0001

Table S3. Parameters of the CPM model for all types of cells (Section 4.2). $\lambda_p$and λ_a are the multipliers of Lagrange corresponding to perimeter and area, respectively, with P_T and A_T representing the target perimeter and area. In brackets are the types of cells. P_S and P_M are the probabilities of cell division occurring for sustentacular (mantle) cells.

Interaction parameters	**Figure 2A (A.U.)**	**Figure 2B (A.U.)**	**Figure 2C (A.U.)**
J_{SS}	*-50*	*50*	*-38*
J_{MM}	*-50*	*50*	*-45*
J_{HH}	*-50*	*50*	*-60*
J_{HM}	*25*	*25*	*5*
J_{SH}	*-25*	*-25*	*-40*
J_{SM}	*-25*	*-25*	*-36*
J_{HO}	*-100*	*100*	*80*
J_{SO}	*-100*	*50*	*56*
J_{MO}	*-100*	*0*	*-10*

Table S4. CPM interaction parameters *J* representing the local binding energies among cells or between cells and their surrounding medium. Values corresponding to Figs. 2 A, B and C, where the latter corresponds to the stable configuration used in all the remaining simulations of this study.

Supplementary Figures

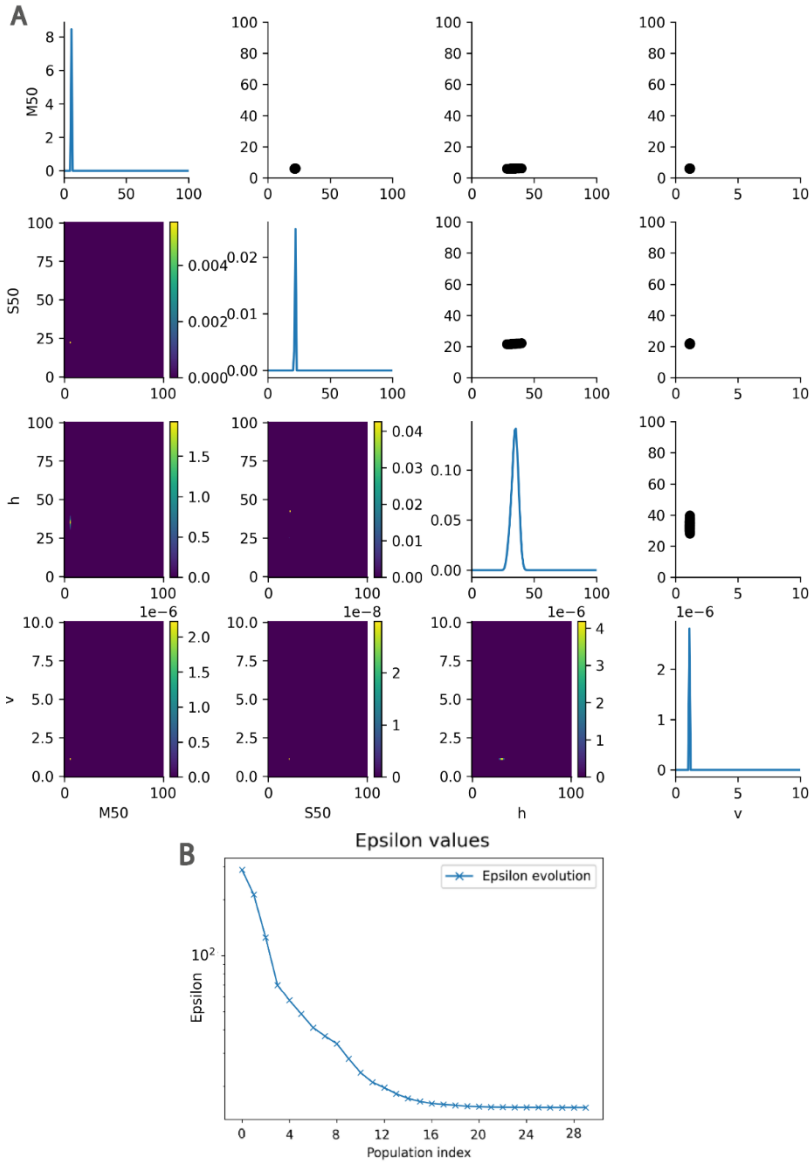

Supplementary Figure S1. Parameter estimation and model fitting using Approximate Bayesian Computation (ABC). (A) Posterior distributions and pairwise correlations of the model parameters M50, S50, h, and v. The distributions were obtained using ABC running until a minimum epsilon of 0.1. The diagonal plots show the posterior distributions of each parameter. The off-diagonal plots display pairwise correlations for pairs: scatter plots and heat maps. M50 represents the half-maximal concentration for mantle cell proliferation, S50 for sustentacular cell proliferation, h is the Hill coefficient, and v is the proliferation rate constant. **(B)** Convergence of the ABC algorithm over successive populations. The epsilon value, which represents the threshold for accepting simulations, decreases with each population, indicating the algorithm's convergence towards the true parameter values. The final epsilon value achieved is 0.1.

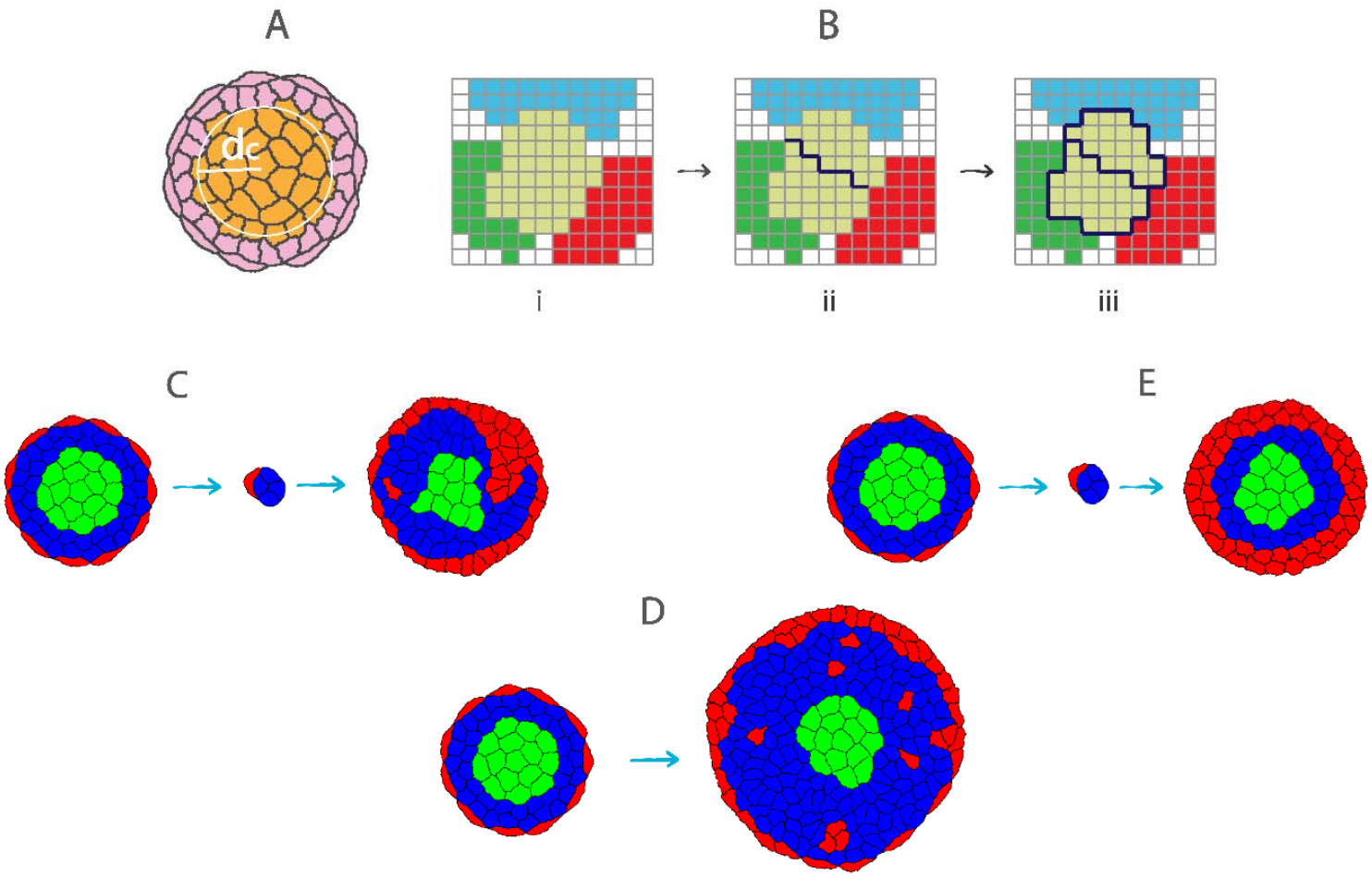

Supplementary Figure S3. Dynamics of cell proliferation during neuromast regeneration. A) Schematic representation of the radial potential governing the cellular differentiation dynamics of sustentacular cells based on a critical distance to the centre of mass referred to as r_c during neuromast regeneration. Within r_c the sustentacular cells differentiate into two hair or two sustentacular cells. However, outside of r_c, the differentiation occurs to two sustentacular, two mantle or one mantle and one sustentacular cells. **B)** Illustration of the implemented cell division process, where a line with a random slope passing through the cellular centre of mass separates the two daughter cells in the next time step. **C)** Simulation results illustrating uninterrupted growth in neuromast regeneration, initiated by retaining only 4-10 cells and simulating during 30000 MCS. **D)** in the absence of ablation, the neuromast exhibits continuous and uninterrupted growth (simulating during 90000 MCS). **E)** Ablation of all but 4-10 cells is followed by cell proliferation regulated by a local "switch" (S) that depends on the number of neighbours, regardless of the cell types. When the number of neighbours is equal or higher than S, proliferation stops. In this example, S = 3 and the time of simulation was 210000 MCS. Parameter values of simulations depicted in C-E in Tables S3 and S4.

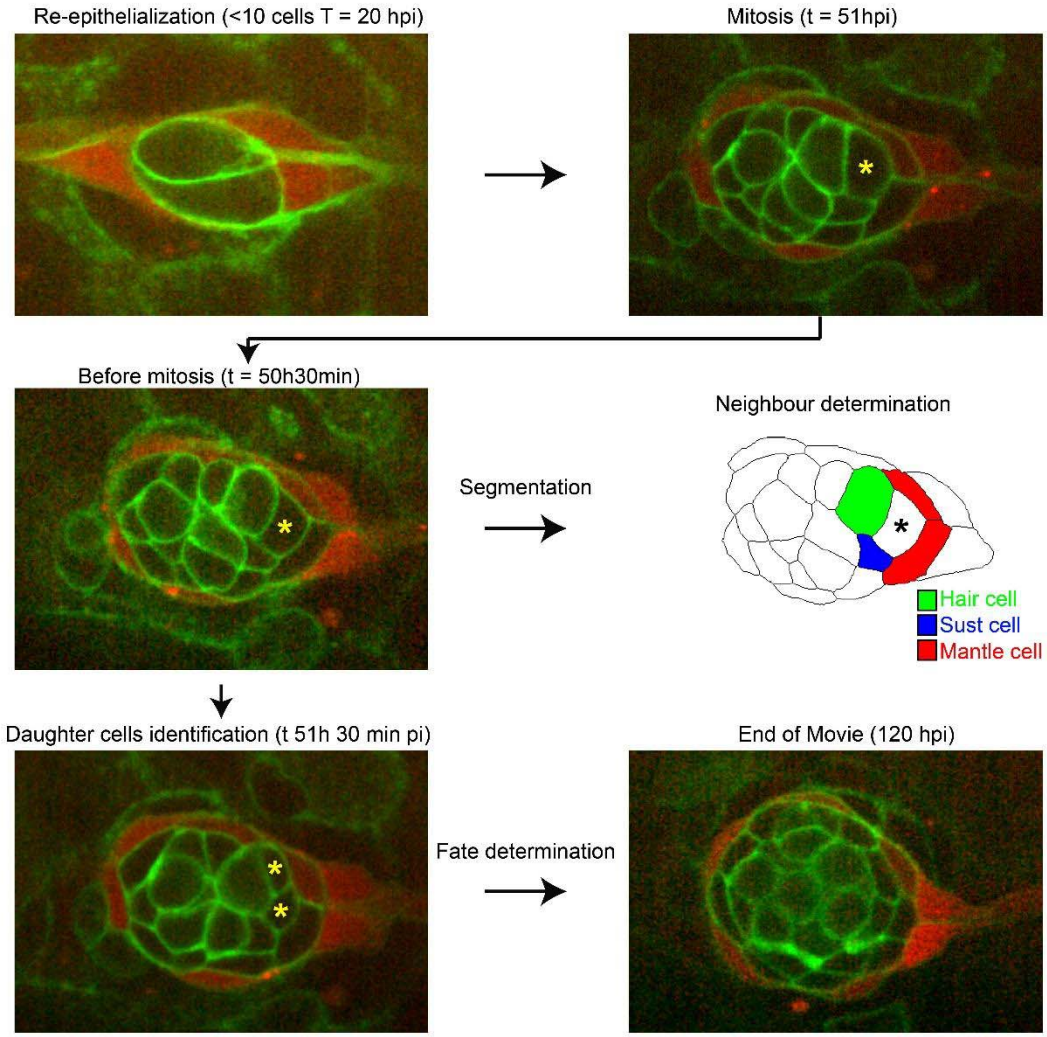

Supplementary Figure S6. Workflow for cell neighbourhood annotation. Cell divisions do not occur in the ~20 hpi as the debris of the death cells are cleared and the tissue re-organizes. For each mitosis in the movie, it is registered the time of division and the final cell-type of the two sibling cells based on morphology and fluorescent markers. Therefore, a dividing cell is classified as HH, SS, MS or MM based on the fate of the progeny (hair cells always appear in pairs, so no dividing cell is HS). For each division, the movie is rewound by 30 minutes, at which point, the neighbours of the dividing cell are identified, as well as their cell type and counted.

Supplementary Movies

Movie S1. Model of an unstable neuromast. Details of model parametrisation described in the legend of Fig. 2 A.

Movie S2. Model of a stable but unrealistic neuromast. Details of the movie described in the legend of Fig. 2 B.

Movie S3. Model of a stable and realistic neuromast. Details of model parametrisation described in the legend of Fig. 2 C.

Movie S4. Model of a growing and regenerating neuromast. Details of model parametrisation described in the legend of Supp. Fig. 3 C.

Movie S5. Model of a growing and uninjured neuromast. Details of model parametrisation described in the legend of Supp. Fig. 3 D.

Movie S6. Model of a regenerating neuromast. Details of model parametrisation described in the legend of Supp. Fig. 3 E.

Movie S7. Model of a regenerating neuromast. Details of model parametrisation described in the legend of Fig. 3 A.

Movie S8. Model of a regenerating neuromast. Details of model parametrisation described in the legend of Fig. 3 B.

Movie S9. Model of a regenerating neuromast. Details of model parametrisation described in the legend of Fig. 3 C.

Movie S10. Model of a regenerating neuromast. Details of model parametrisation described in the legend of Fig. 3 D.

Movie S11. Model of a regenerating neuromast after ablation of the posterior half of the neuromast. Details of model parametrisation described in the legend of Fig. 5 A-B.

Movie S12. Model of a regenerating neuromast after mantle ablation. Details of model parametrisation described in the legend of Fig. 5 C.

Movie S13. Model of a regenerating neuromast after mantle ablation. A representative neuromast regeneration time-lapse. The movie starts 20 hours post ablation when cellular debris has been cleared and the surviving cells, 2 support cells and 3 mantle cells have reattached to one another. Through the 100 hours of the time-lapse the organ recovers cell numbers via proliferation and differentiation occurs, with hair cells appearing from the division of support cells. Frames were taken every 15 minutes. All membranes in the neuromast are marked with Claudnb:lyn-EGFP. Mantle cells are distinguished by a red cytoplasm (alpl:mCherry) and hair cells are further marked by myo6b:ß-actin-GFP. Each time point consist of 14 z-slices 1µm apart but only one z-slice is shown in each frame for clarity.